This article has been accepted for publication in IEEE Transactions on Ultrasonics, Ferroelectrics, and Frequency Control. This is the author's version which has not been fully edited and content may change prior to final publication. Citation information: DOI 10.1109/TUFFC.2024.3443781

Three-dimensional super-resolution passive cavitation mapping in laser lithotripsy

Daiwei Li[1], Nanchao Wang[1], Mucong Li[1], Arpit Mishra, Yuqi Tang, Tri Vu, Gaoming Xiang, Junqin Chen, Michael Lipkin, Pei Zhong, Junjie Yao, *Member, IEEE*

***Abstract*—Kidney stone disease is a major public health issue. By breaking stones with repeated laser irradiation, laser lithotripsy (LL) has become the main treatment for kidney stone disease. Laser-induced cavitation is closely associated with the stone damage in LL. Monitoring the cavitation activities during LL is thus crucial to optimizing the stone damage and maximizing LL efficiency. In this study, we have developed three-dimensional super-resolution passive cavitation mapping (3D-SRPCM), in which the cavitation bubble positions can be localized with an accuracy of 40 μm, which is 1/10th of the acoustic diffraction limit. Moreover, the 3D-SRPCM reconstruction speed has been improved by 300 times by adopting a GPU-based sparse-matrix beamforming approach. Using 3D-SRPCM, we studied LL-induced cavitation activities on BegoStones, both in free space of water and confined space of a kidney phantom. The dose-dependence analysis provided by 3D-SRPCM revealed that accumulated impact pressure on the stone surface has the highest correlation with the stone damage. By providing high-resolution cavitation mapping during LL treatment, we expect that 3D-SRPCM may become a powerful tool to improve the clinical LL efficiency and patient outcome.**

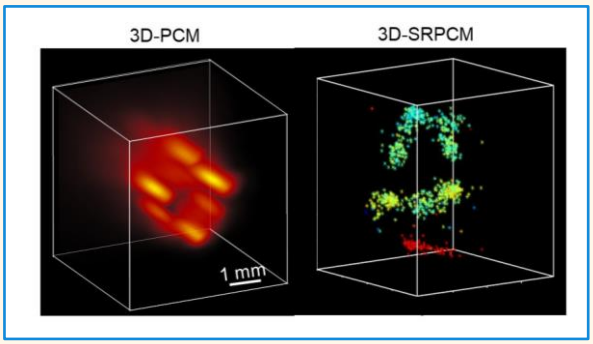

***Index Terms*—Passive cavitation mapping, super-resolution localization, laser lithotripsy, kidney stone disease**

I. Introduction

LASER lithotripsy (LL) has been widely used for clinical treatment of kidney stones [1-3]. The dusting-mode LL has become increasingly popular due to its high fragmenting efficiency and relatively simple procedure without the need for a stent and ureteral access sheath [4-6]. Recent studies have shown that cavitation plays an important role in stone fragmentation in LL [7-9]. Nevertheless, the mechanism of cavitation-induced stone damage during LL remains uncertain [7, 10]. However, our understanding of cavitation mechanisms during LL treatment, as well as further improvement of treatment effectiveness, are hampered by inadequate cavitation characteristics during LL. To this end, it is crucial to map the spatiotemporal distributions of cavitation activities to study how the cavitation activities affect the stone damage [11]. Previous studies have explored various methods for detecting cavitation, such as active cavitation mapping (ACM) [12, 13] and high-speed photograph [14]. For example, Xiang et al. used high-speed photograph to capture cavitation bubble collapse and investigated the transient dynamics of vapor bubbles induced by LL and their correlation with stone damage [15]. Passive cavitation mapping (PCM) has also been demonstrated as a promising technology that provides cavitation monitoring in shockwave lithotripsy [11, 16-18] and other applications [19-21]. We previously developed a 2D-PCM system to image and analyze laser-induced single cavitation bubbles and shock wave-induced cavitation clusters [22]. Using a linear ultrasound transducer array, our 2D-PCM is powered with a sliding-window delay-and-sum reconstruction (SW-DAS) method [22-25].

In clinical settings, it is highly desirable to capture LL-

Manuscript was submitted on May 31, 2024.

[1]Daiwei Li, Nanchao Wang and Mucong Li contribute equally to the work.

Daiwei Li is with the Department of Biomedical Engineering, Duke University, Durham, NC 27708 USA (e-mail: daiwei.li@duke.edu).

Nanchao Wang is with the Department of Biomedical Engineering, Duke University, Durham, NC 27708 USA (e-mail: nanchao.wang@duke.edu).

Mucong Li was with the Department of Biomedical Engineering, Duke University, Durham, NC 27708 USA (email: limucongee@gmail.com).

Arpit Mishra is with the Department of Mechanical Engineering and Materials, Duke University, Durham, NC 27708 USA (e-mail: arpit.mishra@duke.edu).

Yuqi Tang was with the Department of Biomedical Engineering, Duke University, Durham, NC 27708 USA (email: yuqi.tang@duke.edu).

Tri Vu is with the Department of Biomedical Engineering, Duke University, Durham, NC 27708 USA (e-mail: tri.vu@duke.edu).

Gaoming Xiang was with the Department of Mechanical Engineering and Materials, Duke University, Durham, NC 27708 USA (e-mail: gaoming.xiang@duke.edu).

Junqin Chen is with the Department of Mechanical Engineering and Materials, Duke University, Durham, NC 27708 USA (e-mail: jc698@duke.edu).

Michael Lipkin is with the Department of Urology, School of Medicine, Duke University, Durham, NC 27708 USA (e-mail: michael.lipkin@duke.edu).

Pei Zhong is with the Department of Mechanical Engineering and Materials, Duke University, Durham, NC 27708 USA (e-mail: pei.zhong@duke.edu).

Junjie Yao is with the Department of Biomedical Engineering, Duke University, Durham, NC 27708 USA (e-mail: junjie.yao@duke.edu).

Authorized licensed use limited to: Duke University. Downloaded on August 20,2024 at 03:16:54 UTC from IEEE Xplore. Restrictions apply.
© 2024 IEEE. Personal use is permitted, but republication/redistribution requires IEEE permission. See https://www.ieee.org/publications/rights/index.html for more information.

This article has been accepted for publication in IEEE Transactions on Ultrasonics, Ferroelectrics, and Frequency Control. This is the author's version which has not been fully edited and content may change prior to final publication. Citation information: DOI 10.1109/TUFFC.2024.3443781

Highlights

- **Novel 3D-SRPCM method offers high-resolution tracking of cavitation activities during laser lithotripsy.**
- **Our study reveals strong correlation between cavitation activities and stone damage.**
- **3D-SRPCM paves the way for improving kidney stone treatment outcomes through real-time cavitation mapping.**

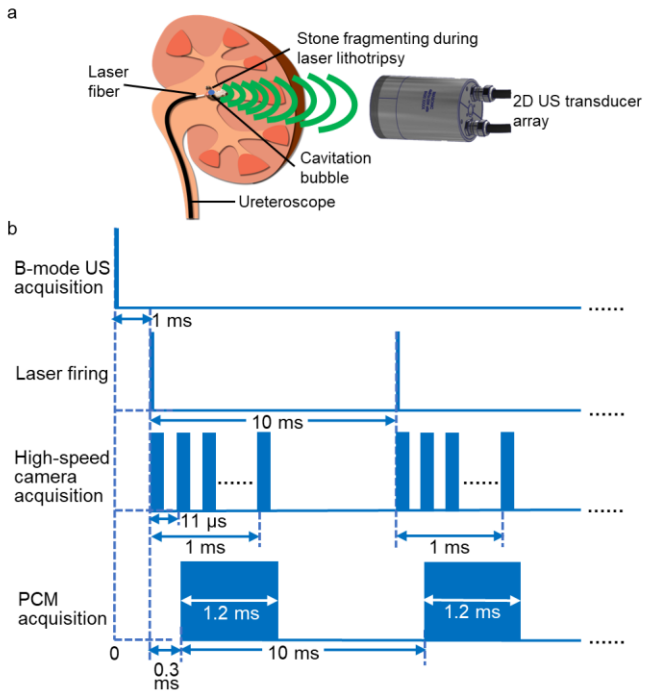

Fig. 1. Schematic of 3D-SRPCM. (a) Diagram of LL-induced cavitation detection with 2D transducer array. (b) Trigger sequence of 3D-SRPCM. The ultrasound B-mode image is acquired before LL laser firing, followed by high-speed camera recording and PCM acquisition.

induced cavitation bubble distribution in three-dimensional (3D) space with high temporal and spatial resolution. In this work, we present 3D super-resolution passive cavitation mapping (3D-SRPCM) that can be seamlessly integrated with ultrasound imaging and clinical LL procedures. Using a semi-spherical ultrasound array, 3D-SRPCM can provide cavitation distribution with a 3D field of view (3D-FOV) of ~8 mm in diameter. A graphics processing unit (GPU) based sparse-matrix delay-and-sum (DAS) beamforming approach was developed for 3D-SRPCM reconstruction, which is 300 times faster than the traditional vector-based DAS method [26]. To further enhance the spatial-temporal resolution, a super-resolution cavitation localization method was developed, which provides the collapse localization with sub-pixel accuracy of 40 µm, as well as a temporal resolution of 0.128 µs [27, 28]. Using 3D-SRPCM, we imaged LL-induced cavitation bubbles in both free space and constricted space. We studied the dose dependence of LL treatment on BegoStones and quantified the correlation between cavitation activities and the stone damage. Collectively, our results have demonstrated the feasibility of 3D-SRPCM during LL treatment, paving the way for future *in vivo* animal and human studies.

II. Methods

A. Configuration of the 3D-SRPCM System

Fig. 1(a) shows the overall diagram of 3D-SRPCM used in free-space LL. To monitor the 3D cavitation activities at the LL fiber tip, we used a customized 2D semispherical ultrasound transducer array (Imasonics, France), which has 256 piezoelectric elements and a central frequency of 4 MHz with a 60% bandwidth. All the transducer elements are uniformly distributed over a spherical surface with a radius of 40.06 mm. The total angular aperture of the array is around 85.8°. The data acquisition was performed by a programmable ultrasound scanner (Vantage 256, Verasonics) with a 15.625 MHz sampling rate. A commercial Holmium:YAG (Ho:YAG) laser lithotripter (H Solvo 35-W laser, Dornier MedTech) was operated with a pulse energy Ep = 0.8 J with a pulse duration of 106 µs and a pulse repetition frequency PRF = 10 Hz. The laser pulse from LL was delivered by using a 365-µm-core-diameter fiber to the stone surface. BegoStone samples (BEGO USA, Lincoln, RI) with similar mechanical properties to human kidney stones were prepared (45×45×5 mm^3) using 5:2 powder to water ratio by weight [29]. The fiber tip was positioned parallel to the stone surface with a stand-off (SD) distance SD = 1.0 mm. The parallel fiber setting was chosen in this study to minimize the photothermal ablation effect. The fiber tip was placed near the focal zone of the semispherical array to capture the bubble collapse around the fiber tip. To validate our SD-SRPCM method, we simultaneously performed high-speed - camera imaging by using a high-speed camera (Vision Research, Wayne, NJ) with a frame rate of 90,909 Hz to record bubble collapse from the side view.

3D ultrasound imaging was conducted before LL treatment to find the positions of the fiber tip and the stone surface. 3D ultrasound images were acquired with a 15-Hz frame rate and a field of view of 8×8×8 mm^3. The triggering sequence of 3D-SRPCM is shown in Fig. 1(b). We synchronized the LL laser pulse firing, high-speed camera recording, PCM acquisition, and 3D ultrasound imaging. The master trigger signal was sent with the laser pulses from LL at 10 Hz. There was a 300-µs delay between the LL trigger and the PCM signal acquisition. The total acquisition time for PCM was 800 µs to capture all the cavitation activities. The high-speed camera acquired 90 images within 1 ms after each laser pulse to capture the whole process of bubble generation and collapse [15].

B. 3D-PCM image reconstruction

LL-induced cavitations can be approximated as sparsely distributed point sources, of which the radiofrequency (RF)

Authorized licensed use limited to: Duke University. Downloaded on August 20,2024 at 03:16:54 UTC from IEEE Xplore. Restrictions apply.
© 2024 IEEE. Personal use is permitted, but republication/redistribution requires IEEE permission. See https://www.ieee.org/publications/rights/index.html for more information.

This article has been accepted for publication in IEEE Transactions on Ultrasonics, Ferroelectrics, and Frequency Control. This is the author's version which has not been fully edited and content may change prior to final publication. Citation information: DOI 10.1109/TUFFC.2024.3443781

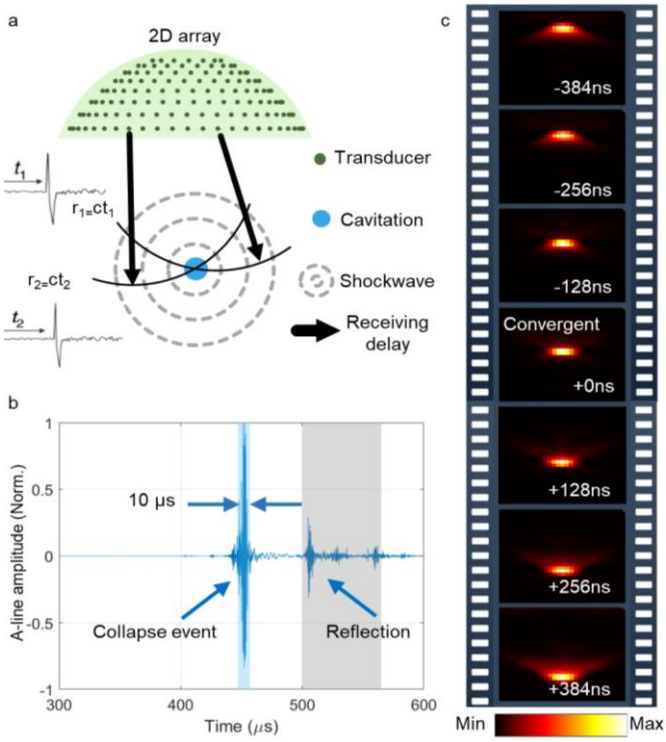

Fig. 2. Illustration of image reconstruction in 3D-PCM. (a) The delay-and-sum beamforming to reconstruct cavitation location. (b) Automatic identification of the collapse event (the shaded blue) and the reflection (the shaded gray). (c) The series of reconstructed PCM images with varied starting time points.

signals are recorded by the 2D semispherical transducer array, as shown in Fig. 2(a). As in our previously reported work, if we know the exact time of each bubble collapsing, the 3D-PCM image can be reconstructed by using the delay-and-sum (DAS) beamforming method [16, 25]:

$$A(\vec{r},t_s)=\sum_{n=1}^{N}\alpha_n\left(\vec{r}\right)\cdot S_n\left(t_s+\frac{\left|\vec{r}-\vec{r_n}\right|}{c}\right), \quad (1)$$

where A is the reconstructed acoustic pressure at the location $\vec{r}$ and the collapsing time t_s; $\alpha_n$refers to the angular sensitivity of the n-th transducer element at the location $\vec{r}$; S_n denotes the RF signal contributed from the location $\vec{r}$ to n-th transducer element at $\vec{r_n}$ after the propagation time $\frac{|\vec{r}-\vec{r_n}|}{c}$; c is the speed of sound. Note that the pressure amplitude is proportional to the cavitation strength.

Since the bubble collapsing time t_s is unknown, we have introduced a two-step method that searches for the optimized starting time point (STP). First, automatic peak searching is applied to the RF data recorded by the center transducer element [30], which estimates the approximate time for the cavitations collapses. The typical bubble dynamics with SD = 1.0 mm include jet impact and non-circular toroidal bubble collapse, following the primary and secondary bubble collapses (*i.e.,* a collapse event as shown in Fig. 2(b)) [15]. Usually, multiple bubbles collapse within a period of ~10 μs. RF signals with relatively low intensities and short intervals are identified as reflection signals from the stone surface. Second, for each cavitation collapse, a series of images are reconstructed by using the 3D SW-DAS method with different STPs, shown in

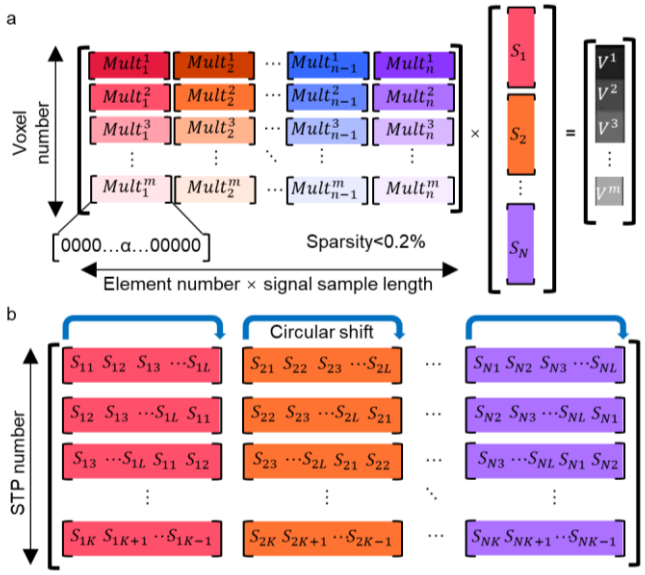

Fig. 3. Illustration of (a) the reconstructed sparse matrix and (b) the stacked RF data for page-wise sparse-matrix multiplication. STP: starting time point.

Fig. 2(c) [22, 25]. Using the SW-DAS images, we can find the true collapsing time which results in the most converged image of the bubble. Therefore, the temporal resolution of 3D-PCM is determined by RF signal sampling rate. The spatial resolution of 3D-PCM is limited by acoustic diffraction. Nevertheless, SW-DAS is time-consuming for investigating the detailed bubble dynamics. Furthermore, precise cavitation localization beyond the acoustic diffraction is needed for studying the spatial dependence of the stone damage. To address these challenges, we have developed techniques to accelerate the 3D-PCM image reconstruction and improve the spatial resolution, as detailed in the following sections.

C. Page-wise GPU-based sparse-matrix DAS beamforming

To speed up 3D-PCM reconstruction, we have developed a page-wise, sparse-matrix-multiplication, and GPU-based method. First, we adapt sparse matrix multiplication which is faster than vector-based DAS [26, 31]. The sparse matrix can reduce memory usage and speed up the processing as it only stores the non-zero elements. Second, we stack the RF data sequences with different STPs into a hybrid matrix with multiple pages, allowing for sparse matrix multiplication for multiple beamforming instances. Third, we perform sparse matrix multiplication using a GPU (NVIDIA® GeForce RTXTM 3090) that can offer parallel processing with high computational throughput.

For better clarity, we describe the construction of the sparse matrix prior to beamforming. We can rewrite Eq. (1) into the matrix format:

$$A(V^m)=\sum_{n=1}^{N}Mult_n^m\cdot S_n=Mult^m\cdot S, \quad (2)$$

where A denotes the reconstructed pressure amplitude at the voxel V^m as in Eq. (1); $Mult_n^m$ is a vector of $1\times L$ with the same length L as the single-channel RF samples S_n $(L\times 1)$, and it only contains one single non-zero component determined

Authorized licensed use limited to: Duke University. Downloaded on August 20,2024 at 03:16:54 UTC from IEEE Xplore. Restrictions apply.
© 2024 IEEE. Personal use is permitted, but republication/redistribution requires IEEE permission. See https://www.ieee.org/publications/rights/index.html for more information.

This article has been accepted for publication in IEEE Transactions on Ultrasonics, Ferroelectrics, and Frequency Control. This is the author's version which has not been fully edited and content may change prior to final publication. Citation information: DOI 10.1109/TUFFC.2024.3443781

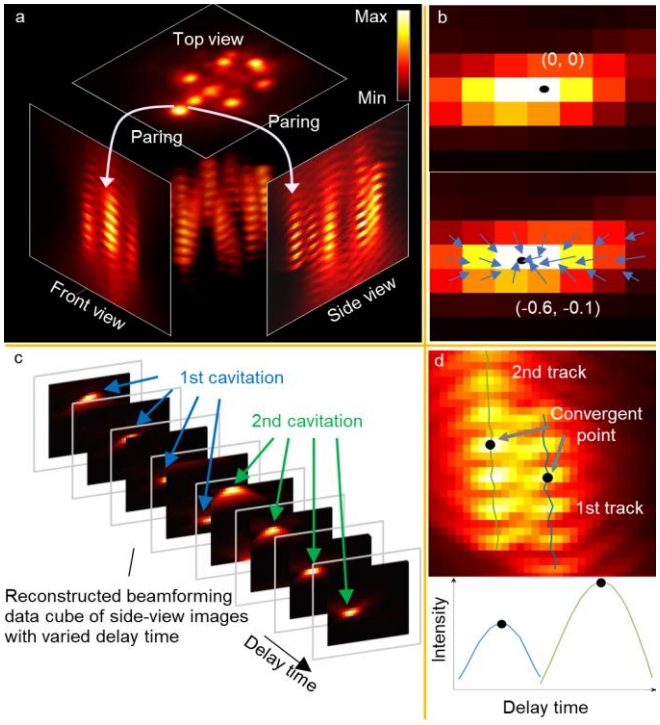

Fig. 4. Illustration of 3D super-resolution (SR) cavitation localization. (a) The delay-time lapsed 3D image volume is projected into 2D maximum intensity projections to enhance efficiency. (b) The mechanism of the radial symmetric method for 2D SR localization. (c) An example of localizations of the delay-time lapsed 2D images from two cavitations. (d) An example to track the converging points for two cavitations.

by the distance between n-th transducer element and the voxel V^m. Additionally, the non-zero component includes the angular sensitivity of the n-th transducer element with regard to the voxel V^m. Next, by stacking the vector $Mult_n^m$ and the RF data S_n over all the transducer elements, A can be generated by multiplying two stacked matrixes. By repeating the operation for all elements, we can establish a sparse matrix ($M \times NL$, Fig. 3(a)) for a single DAS beamforming. Here, we assume the total number of STPs is K (*i.e.*, the page number). To further accelerate the reconstructions with varied STPs, the RF data of each channel is shifted circularly to keep the same sample size (Fig. 3(b)) and stacked into a multiple-page matrix ($N \times L \times K$). Then, we rearrange the continuous set of transformed RF data into a Casorati matrix ($NL \times K$, Fig. 3(b)). The outcome of multiplication between the sparse matrix and the stacked circular shifting RF data is reshaped into a series of 3D PCM images of $N_x \times N_y \times N_z \times K$, where N_x, N_y, and N_z denote the pixel numbers of the reconstructed FOV along x, y, and z.

D. 3D super-resolution cavitation localization

LL-induced cavitation bubbles can be approximated as point sources. Super-resolution cavitation localization can be performed to extract the bubble collapse position. It is similar with 3D particle trajectory tracking—if we consider the cavitation event as a single particle [27, 32]. Hence, we modified the 2D particle trajectory tracking method on the maximum intensity projection (MIP) of the 3D-PCM images, and combined the 2D tracking results from different MIP views to generate 3D trajectories of a single cavitation (Fig. 4 (a)).

The radial symmetric (RS) method was adopted that could provide SR localization with a sub-pixel accuracy of approximately 1/10 of the diffraction-limited resolutions [33]. The RS method assumes that the cavitation signal is radially symmetric. In other words, all gradient vectors at each pixel point to the cavitation center (Fig. 4(b)). For noisy images, this approach aims to minimize the total distance between the optimized center point and all gradient vectors [34]. After storing the center positions of cavitations reconstructed with increasing STPs (Fig. 4(c)), the tracking was implemented based on the Kuhn-Munkres (KM) algorithm [35]. The 2D distances from all cavitations between two STP images were calculated. By applying the KM algorithm, the optimal pairing between two STP images was achieved by minimizing the total distance. Repeating this process over STPs, the 2D trajectories of all cavitation events were generated to identify the most converging time points for each cavitation (Fig. 4(d)).

To extract 3D trajectories, the tracks from three-view MIP images were generated. A generalized distance between the tracks from different views was computed as:

$$Dis(I,J)=\frac{1}{L_{T_I\cap T_J}}\sum_{T_i=T_j}\sqrt{C_A\cdot\frac{\left(A_i-A_j\right)^2}{\left(\arg\max_{n\in T_I\cup T_J}A_n\right)^2}+C_X\cdot\frac{\left(X_i-X_j\right)^2}{\left(\arg\max_{n\in T_I\cup T_J}X_n\right)^2}}, \quad (3)$$

where I and J are two 2D tracks to be paired; L is the total length of track after paring; T denotes the STP of each element in the track. Note that we only considered those tracks from different views with the same STPs for comparison. For the elements with the same STPs in two tracks, the normalized deviations were calculated including the localized central amplitude and the center position. The subscripts i and j indicate the elements corresponding to track I and J from different views. Note that the values of A_n and X_n for normalization is generated from the two paring tracks. C_A and C_X are the hyper parameters to adjust the pairing sensitivities to amplitude and position, respectively. By applying the generalized distance and KM algorithm, the track pairing process was able to reliably identify the same cavitation track from three-view MIP images. If two closely distributed cavitations overlap in one MIP view, only two MIP views were paired. Consequently, the 3D cavitation information (including intensity, positions, and collapsing time) was extracted by combining the paired 2D tracks.

E. Kidney Phantom and Experiment Setup

The LL-induced bubble collapse monitoring experiments were conducted both in the free space like water tank, and also the confined space as anatomically realistic kidney phantom. The protocol for making the kidney phantom was reported in our previous publication [36]. The kidney phantom was molded with transparent hydrogel (Gelatin #1, Humimic Medical, SC, USA), providing high optical and acoustic transparency. The kidney phantom structures were simplified while maintaining anatomical accuracy. We split the kidney phantom in two haves (Fig. 5(a)). A 3D-printed frame was used to hold the two halves. The phantom had three accessible regions: the pelviureteric junction (PUJ), upper pole, and lower pole, with a volume of 1.12 cm^3 , 1.63 cm^3, and 0.61 cm^3, respectively [36]. Additionally, cylindrical channels were added to facilitate the insertion of the stone and the passage of stone fragments and fluid (Fig. 5(b)).

Authorized licensed use limited to: Duke University. Downloaded on August 20,2024 at 03:16:54 UTC from IEEE Xplore. Restrictions apply.
© 2024 IEEE. Personal use is permitted, but republication/redistribution requires IEEE permission. See https://www.ieee.org/publications/rights/index.html for more information.

This article has been accepted for publication in IEEE Transactions on Ultrasonics, Ferroelectrics, and Frequency Control. This is the author's version which has not been fully edited and content may change prior to final publication. Citation information: DOI 10.1109/TUFFC.2024.3443781

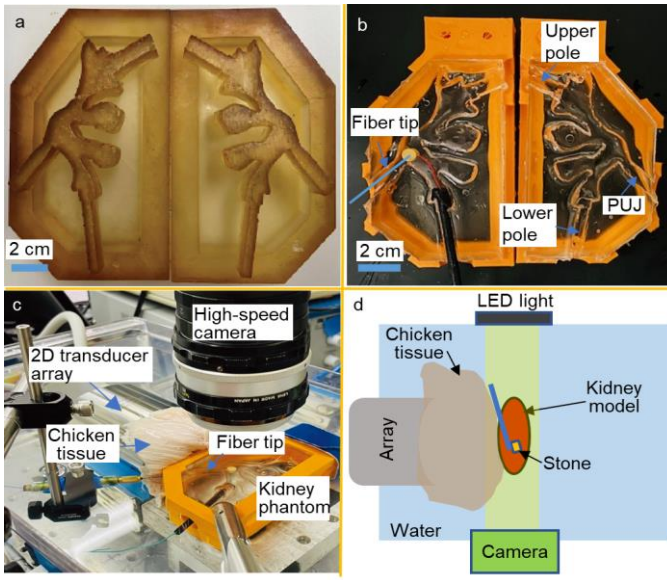

Fig. 5. Kidney phantom and experiment setup. (a) Picture of kidney phantom model. (b) Picture of kidney phantom with outer frame. A Bego stone was inserted. (c) Picture of kidney phantom experiment setup. (d) Schematic of kidney phantom experiment setup from the side view.

Fig. 5(c)-(d) show the LL experiment setup in the kidney phantom. A cylindrical BegoStone with a diameter of 6 mm and a length of 3 mm tethered to a soft wire was inserted into the renal pelvis. The stone's flat surface was placed in the focal zone of the 2D transducer array. The LL fiber tip was inserted through the renal pelvis. High-speed camera was placed on the top of the kidney phantom to record the bubble activities. A layer of 2-cm-thick chicken tissue was placed between the 2D transducer array and the kidney phantom, mimicking the acoustic attenuation in biological tissues. We were not able to further increase the tissue thickness, limited by the focal length of the ultrasound transducer array.

III. Experimental Results

A. Validation of 3D-SRPCM on Single Bubbles

We first conducted characterization experiments for the 2D transducer array as shown in Fig. 6. All the elements in the 2D transducer array point to the center of the geometric sphere, forming a spherical FOV with the highest detection sensitivity. A microbead was embedded in agarose gel and excited by a pulse laser at 532 nm. The resultant photoacoustic signals from the microbead mimicked the cavitation signals. The photoacoustic signals were acquired with the microbead translated over a distance of 50 mm (laterally) by 20 mm (axially). Fig. 6(a) shows the assembled images of the microbead at different locations. The detection sensitivity and the spatial resolution of the 2D transducer array deteriorate from its geometric center, with a −6 dB focal zone of ~8 mm in diameter. The diffraction-limited spatial resolutions of the 2D transducer array at the center was 433 μm (x-axis), 440 μm (y-axis) and 186 μm (z-axis), as shown in Fig. 6(b).

We then conducted the single-bubble experiment with 3D-SRPCM. A nanosecond laser beam was focused into water through a convex lens (NA = 1.0), resulting in a ~0.81 μm optical focal spot, which was used as the ground truth of the

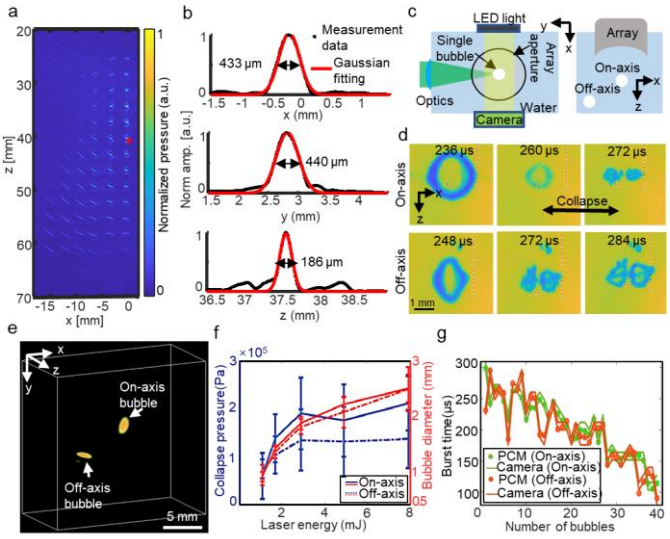

Fig. 6. Characterization of the 2D transducer array and single-bubble validation of 3D-SRPCM. (a) Photoacoustic signal from the microbead at different positions. x=0 marks the central acoustic axis of the array. (b) In-focus diffraction-limited spatial resolutions of the 2D transducer array. (c) Experiment setup of on-axis and off-axis single-bubble detection. (d) Bubble dynamics captured by the high-speed camera. (e) Example 3D-SRPCM image of the on-axis and off-axis single-bubbles. (f) 3D-SRPCM pressures and camera-captured bubble diameters at different laser energy levels. (g) Bubble collapse time by 3D-SRPCM and high-speed camera.

bubble location. A single bubble was produced per laser pulse at the optical focus due to the optical breakdown. The first group of bubbles were generated 40 mm in depth along the z axis of the 2D transducer array. The second group of bubbles were generated 15 mm off the z axis. Five different laser pulse energy levels (1 mJ, 2 mJ, 3 mJ, 5 mJ and 8 mJ) were employed, producing different bubble sizes. For each energy level, eight bubbles were recorded. The bubble size and collapsing location were also measured by the high-speed camera. The experimental setup is shown in Fig. 6(c).

A series of representative camera images are shown in Fig. 6(d). Fig. 6(e) shows the bubble collapse images acquired by 3D-SRPCM. The measured collapse pressure and the bubble size for on-axis and off-axis bubbles are shown in Fig. 6(f). Both the bubble sizes and collapse pressure increased with the laser pulse energy. Limited by surface tension, the bubble size and collapse pressure reached a plateau when laser pulse energy was above 5 mJ. The collapse time of all 80 bubbles captured by the camera and 3D-SRPCM were consistent, as shown in Fig. 6(g). By comparing the collapse locations of all 80 bubbles acquired by the high-speed camera and the 3D-SRPCM, we found that the average localization accuracy of 3D-SRPCM is ~40 μm, which is about 1/10 of the acoustic diffraction limit of the 2D transducer array.

B. Processing Speed of 3D-SRPCM

Fig. 7(a) shows an example of 3D ultrasound image of a flat square BegoStone with a parallel LL fiber, 3D-PCM reconstruction image, and 3D-SRPCM bubble collapse localization image. The 3D-PCM image has a reconstruction volume of 5 mm × 5 mm × 5 mm and a pixel size of 80 μm. We compared our GPU-based page-wise beamforming algorithm with traditional methods (Fig. 7(b)). The CPU is

Authorized licensed use limited to: Duke University. Downloaded on August 20,2024 at 03:16:54 UTC from IEEE Xplore. Restrictions apply.
© 2024 IEEE. Personal use is permitted, but republication/redistribution requires IEEE permission. See https://www.ieee.org/publications/rights/index.html for more information.

This article has been accepted for publication in IEEE Transactions on Ultrasonics, Ferroelectrics, and Frequency Control. This is the author's version which has not been fully edited and content may change prior to final publication. Citation information: DOI 10.1109/TUFFC.2024.3443781

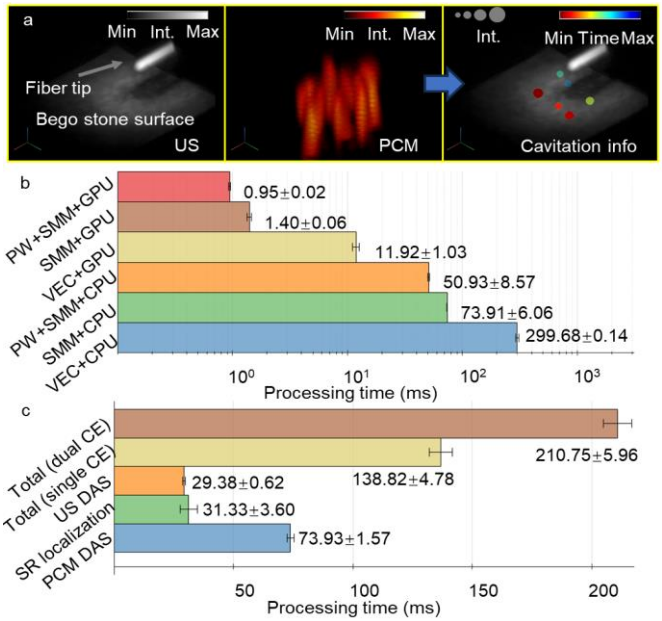

Fig. 7. Processing speed of 3D-SRPCM. (a) Representative ultrasound B-mode image, 3D-PCM image, and 3D-SRPCM image of cavitation activities on a flat BegoStone surface with a parallel LL fiber. (b) The beamforming speed by using different methods. PW: page-wise; SMM: sparse-matrix multiplication; VEC: vectorized operation. (c) The processing time of 3D-SR-PCM by using the GPU-based page-wise sparse-matrix beamforming algorithm. CE: collapse event.

Intel® CoreTM i9-12900K and the GPU is NVIDIA® GeForce RTXTM 3090. The GPU-based page-wise sparse matrix beamforming has the shortest processing time of <1 ms, which is >300 times faster than the traditional vectorized CPU-based method. The most significant improvement is achieved by applying GPU-accelerated sparse-matrix multiplication. It is interesting to note that the page-wise data assembly has a larger impact on GPU (8.51 times faster) than on CPU (4.05 times faster). Using the GPU-based page-wise sparse-matrix beamforming algorithm, we evaluated the total processing speed of the entire 3D-SRPCM pipeline for a single laser pulse from LL (Fig. 7(c)). The processing time is 29.38±0.62 ms for the ultrasound reconstruction, 73.93±1.57 ms for 3D-PCM reconstruction, and 31.33±3.60 ms for localization in 3D-SRPCM. Thus, the total processing time for a single collapse event in 3D-SRPCM is ~140 ms.

C. 3D-SRPCM with Single LL Pulse

We tested 3D-SRPCM with a single LL pulse. Different from the single bubble by the optical breakdown at the optical focus, the bubbles generated by a LL pulse are spread out near the stone surface. Based on our previous study using a Ho:YAG laser [15], we chose SD = 1.0 mm to produce relatively large bubbles. The long LL pulse and solid boundary interaction create an elongated "pear-shaped" bubble that collapses asymmetrically and forms multiple water jets in sequence. The high-speed camera images of bubble generation and collapse were shown in Fig. 8(a). Between 0 to 351 µs after the laser pulse, the cavitation bubble was generated and expanded to its maximum size. The first collapse (jet impact and toroidal bubble collapse in sequence) happened between 702 µs and 729 µs and the second collapse (rebound bubble collapse) happened between 972 µs and 999 µs. There were multiple collapse

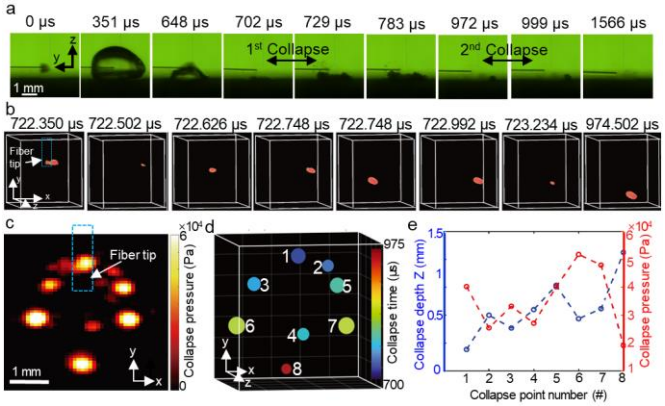

Fig. 8. 3D-PCM and 3D-SRPCM of LL-induced cavitation with a single laser pulse. (a) Bubble dynamics captured by the high-speed camera (scale bar: 1mm). (b) 3D-PCM images of 8 collapse bubbles. (c) The x-y maximum amplitude projection image of 3D-PCM results (scale bar: 1mm). (d) 3D-SRPCM image of the 8 collapse bubbles, color-coded by the collapse time. (e) Collapse depth and pressure of each bubble.

events which were not resolved by the camera due to its limited temporal resolution. Fig. 8(b) shows eight individual collapse events reconstructed by 3D-PCM, showing much higher temporal resolution than the high-speed camera. For example, 3D-PCM distinguished toroidal bubble collapses between 702 µs and 729 µs. Fig. 8(c) shows the maximum amplitude projection (MAP) of the accumulated cavitation intensity of all eight collapse events, as reconstructed by 3D-PCM. It can be observed that the collapse intensity was highly location dependent near the stone surface. The super-resolution localization of the bubbles by 3D-SRPCM were shown in Fig. 8(d), providing much higher accuracy than 3D-PCM. In the 3D-SRPCM image, the center of the sphere represents the collapse location of each cavitation event, and the color of the spheres is coded by their collapsing time. The classic self-intensified phenomenon can be observed from the 3D-SRPCM results [15]. The toroidal bubbles collapse started from the fiber tip and then followed a quarter arc to both sides. Quantitative analysis from the 3D-SRPCM results was shown in Fig. 8(e). Cavitations at location #6 and #7 had the highest collapse pressure, while cavitation at location #1 was the closest to the stone surface (i.e., smallest collapse depth). This experiment demonstrated that 3D-SRPCM is capable of mapping the individual cavitation events induced by laser pulses from LL, with higher temporal resolution than the high-speed camera and higher spatial resolution than 3D-PCM.

D. 3D-SRPCM with Accumulated LL Pulses

Dose-dependence in LL refers to the relationship between the accumulated laser energy delivered to the target stone and its effect on the stone. Using 3D-SRPCM, we can study the accurate location and time of bubble collapse and analyze the correlation between the accumulated cavitation activities with the stone damage, allowing for better understanding of LL-induced cavitation and optimized treatment parameters. To study the dose-dependence during LL treatment, we treated the flat surface of the BegoStone with different pulse numbers (pN), ranging from 10 to 100 pulses with the same laser setting. Similar to the single LL pulse experiment, ultrasound B-mode images were acquired before each treatment. 3D-SRPCM and

Authorized licensed use limited to: Duke University. Downloaded on August 20,2024 at 03:16:54 UTC from IEEE Xplore. Restrictions apply.
© 2024 IEEE. Personal use is permitted, but republication/redistribution requires IEEE permission. See https://www.ieee.org/publications/rights/index.html for more information.

This article has been accepted for publication in IEEE Transactions on Ultrasonics, Ferroelectrics, and Frequency Control. This is the author's version which has not been fully edited and content may change prior to final publication. Citation information: DOI 10.1109/TUFFC.2024.3443781

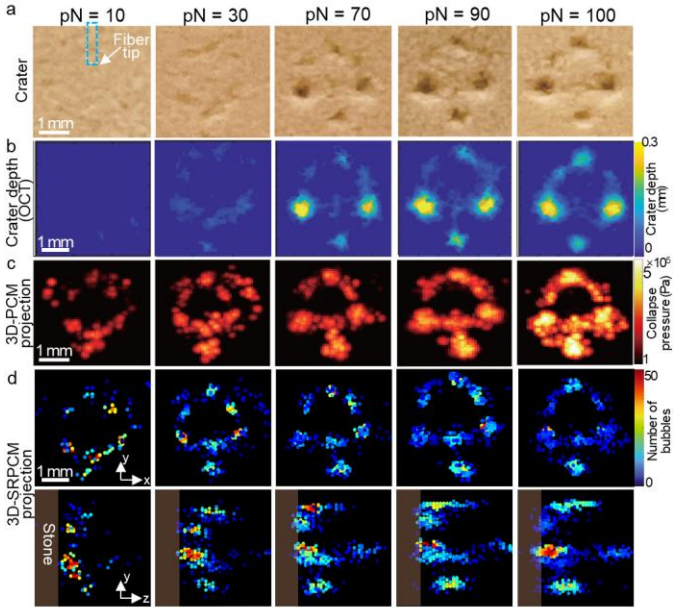

Fig. 9. 3D-SRPCM of accumulated LL-induced cavitations. (a) Pictures of craters on stone surface with different pulse number (pN) (scale bar: 1mm). (b) OCT images of the crater with different pulse numbers (scale bar: 1mm). (c) Maximum amplitude projections of collapse pressure at the x-y plane, acquired by 3D-PCM (scale bar: 1mm). (d) 3D-SRPCM images of the individual bubbles projected at the x-y plane and y-z plane, with the bubble density color-coded from sparse (blue) to condense (red).

high-speed camera were used to monitor each treatment. After each treatment, we used optical coherence tomography (OCT) to measure the LL-generated craters on the stone surface. Fig. 9(a) shows the stone surface treated with different pNs. The craters were distributed along an arc pattern near the fiber tip, with the two largest craters on the side of the fiber tip and another major crater at the far end. The OCT images are shown in Fig. 9(b), from which the crater depth, size, and volume were quantified. As shown in Fig. 9(c), the 3D-PCM images reflect the accumulated cavitation pressure distribution. For pN =10 and 20, although the accumulated cavitation pressure maps showed the arc pattern around the fiber tip, there were no significant craters formed on the stone surface. The 3D-SRPCM results are shown in Fig. 9(d), providing accurate location and time of each cavitation bubble, consistent with the crater pattern on stone surface quantified by OCT. It is worth noting that 3D-SRPCM also resolved the bubbles inside the crater, which were shown below the stone surface in Fig. 9(d). More analysis of the dose-dependent cavitation activities is provided in the next section.

E. Dose-dependence Analysis

From the dose-dependence 3D-SRPCM results in Fig. 9(d), we analyzed the cavitation characteristics and studied their correlation with the stone damage. It is worth noting that super-resolution localization in 3D-SRPCM is critically important for analyzing the cavitation characteristics on the bubble-by-bubble basis, such as the collapse location, impact pressure, and spatial bubble density. Fig. 10(a) shows the accumulated collapse location of the 100 LL pulses. Approximately 800 bubbles were grouped into seven locations labeled as A to G. Fig. 10(b) shows the 3D cavitation density distribution. It can

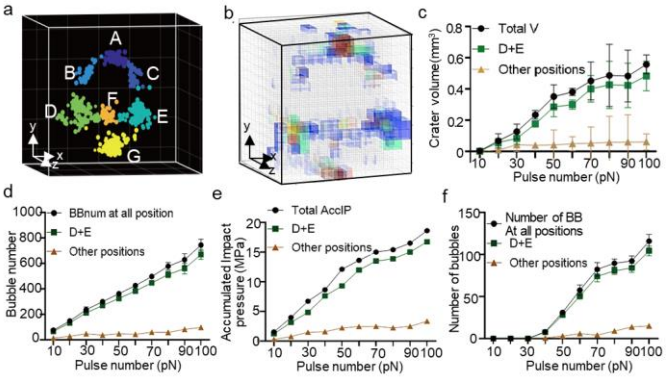

Fig. 10. Dose-dependence analysis by 3D-SRPCM. (a) Accumulated collapse location of ~800 bubbles, which were grouped into 7 positions from A to G. (b) Accumulated 3D bubble density distribution. (c) Dose-dependence of crater volume (V) by OCT. (d) Dose-dependence of bubble number (BBnum). (e) Dose-dependence of accumulated impact pressure (Acc IP). (f) Dose-dependence of bubble density.

be observed that the cavitation densities at positions A, D, E and G were higher than the other positions, consistent with the crater volume in Fig. 9(b). The dose-dependent crater volumes at different locations were shown in Fig. 10(c). Fig. 10(d)-(f) illustrate the dose-dependent accumulated bubble number, accumulated impact pressure (Acc IP), and cavitation density at various locations. Here, impact pressure on the stone surface is quantified based on the cavitation pressure on the transducer surface and the cavitation-stone distance. In general, all the cavitation characteristics from 3D-SRPCM are highly location-dependent and have shown positive-dependence on the pulse number pN. The total bubble number has approximately linear dependence on pN, while Acc IP and cavitation density have multi-phased dependence on pN. The dose-dependence results indicate that the accumulated effects of cavitation activities on the stone damage are not a linear process. There is clearly a threshold effect that requires a minimal number of 30 laser pulses from LL to generate a visible impact on the stone surface (Fig. 9(a)). The accumulated damage on the stone surface is noted to modulate the dynamics of bubble collapse and damage progression during laser lithotripsy. This suggests that the mechanical properties of the stone, such as its hardness or composition, can influence the formation and evolution of craters during the cavitation process [15].

We also analyzed the correlation between the cavitation characteristics and the stone damage (*i.e.,* the crater characteristics). Here, we used the Spearman's correlation coefficient that assesses how well the relationship between two variables can be described using a monotonic function. Shown in Fig. 11(a), we assessed the Spearman's coefficients between the main crater characteristics (volume, depth, and averaged cavitation distance to the stone surface (AVE Depth), accumulated cavitation pressure on the transducer surface (Acc P), accumulated impact pressure on the stone surface (Acc IP), averaged collapse pressure (AVE P), averaged impact pressure area) and the main cavitation characteristics, including the on the stone surface (AVE IP), and total number of bubbles in one treatment (Total BBnum). The coefficient map reveals that the accumulated impact pressure (Acc IP) had the highest correlation coefficient of 0.93 with the crater volume, while the averaged pressure (AVE P) had the least correlation of 0.17

Authorized licensed use limited to: Duke University. Downloaded on August 20,2024 at 03:16:54 UTC from IEEE Xplore. Restrictions apply.
© 2024 IEEE. Personal use is permitted, but republication/redistribution requires IEEE permission. See https://www.ieee.org/publications/rights/index.html for more information.

This article has been accepted for publication in IEEE Transactions on Ultrasonics, Ferroelectrics, and Frequency Control. This is the author's version which has not been fully edited and content may change prior to final publication. Citation information: DOI 10.1109/TUFFC.2024.3443781

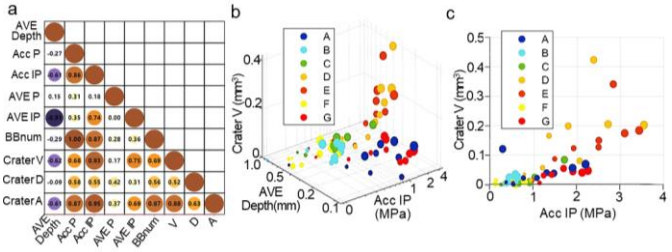

Fig. 11. Correlation analysis between stone damage and cavitation characteristics by 3D-SRPCM. (a) Spearman's correlation map between cavitation characterizations and crater damage. AVE Depth: averaged cavitation distance to the stone surface; Acc P: accumulated cavitation pressure on the transducer surface; Acc IP: accumulated impact pressure on the stone surface; AVE P: averaged collapse pressure; AVE IP: averaged impact pressure on the stone surface; Total BBnum: total number of bubbles in one treatment; V: crater volume; D: maximum crater depth; A: crater area. (b) Scatter plot of averaged collapse depth, accumulated impact pressure, and the crater volume. (c) Scatter plot of accumulated impact pressure and the corresponding crater volume.

with the crater volume. We further analyzed the location-dependence of the correlation between the AVE Depth/Acc IP and the crater volume (Fig. 11(b)), clearly showing that stronger Acc IP and larger AVE Depth resulted in larger crater volume, for example, at position D and E. Moreover, we highlighted the strong correlation between Acc IP and the crater volume in Fig. 11(c), indicating that mechanical fracturing instead of the photothermal effect is the dominating factor for the stone damage in Ho: YAG LL.

F. 3D-SRPCM of LL Treatment in a Kidney Phantom

To mimic the clinical setting, the 3D-SRPCM system was applied for LL in a constrained space inside a kidney phantom. Fig. 12 shows representative 3D-SRPCM results with 100 LL pulses. A fish-shaped crater was formed around the fiber tip as shown in Fig. 12(a), which was confirmed by the OCT image as shown in Fig. 12(d). The high-speed camera captured the bubble collapsing dynamics in Fig. 12(b) and the treatment process was recorded by the endoscope camera in Fig. 12 (c). The 3D-PCM intensity map was consistent with the crater shape in Fig. 12(e), which, however, cannot resolve the individual cavitation locations. The 3D-SRPCM results, on the other hand, can clearly distinguish the bubble localizations generated by each laser pulse (Fig. 12(f)). According to our dose-dependency study in Fig, 10, we analyzed 8 groups of 3D-SRPCM data sets performed in the kidney phantom and quantified the correlation between Acc IP and crater volume V (Fig. 12(g)), as well as total bubble numbers (BB num) and crater volume V (Fig. 12(h)). Again, both Acc IP and BB num have strong correlation with the crater volume. It is worth noting that the smiling-face-shaped crater pattern in the parallel fiber setting was not generated in the kidney phantom experiment. This is mainly because during the LL treatment inside the kidney phantom, the angle of the fiber tip and the SD were not consistent.

IV. Discussions

Cavitation is an important mechanism for stone damage during LL treatment of kidney stone disease. In this work, we used the parallel fiber setting to minimize thermal ablation and maximize the contribution of cavitation activities. Our 3D-

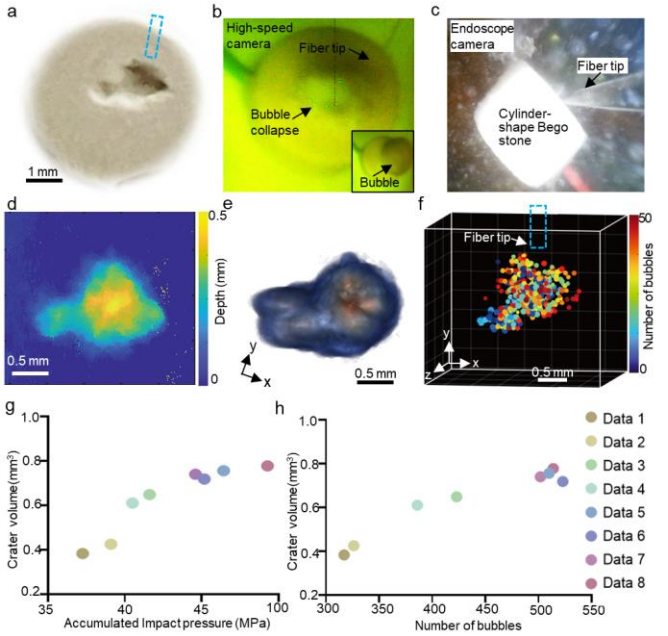

Fig. 12. 3D-SRPCM of LL-induced cavitation in a kidney phantom. (a) Picture of the crater on the stone surface. The location of the fiber tip was marked by the blue box. (b) Picture of bubble collapse (and the maximum bubble generation on the right bottom) captured by high-speed camera. (c) Screenshot of the video recording captured by the endoscope camera. (d) The crater depth map by OCT. (e) 3D-PCM image of the accumulated cavitation pressure. (f) 3D-SRPCM bubble density image of all individual cavitation bubbles, with the bubble density color-coded from sparse (blue) to dense (red). (g) Scatter plot of 8 different data sets of crater volume and accumulated impact pressure from 3D-SR-PCM. (h) Scatter plot of 8 different data sets of crater volume and bubble density.

SRPCM system was demonstrated for localizing the cavitation bubbles with the parallel fiber setting. Vertical and tilted fiber orientation settings will be investigated in future work. A representative SD of 1 mm and laser pulse rate of 10 Hz were used in our experiments in this work. To evaluate the correlation between stone damage and cavitation activities, more correlation studies with a stone damage prediction model will be conducted under different laser conditions, which can provide more information for assessing the effectiveness of the treatment procedure.

3D-SRPCM provides high-resolution mapping of the cavitation bubble bursting based on the assumption that the cavitation bubbles are sparsely distributed both in time and space. Nevertheless, 3D-SRPCM cannot distinguish the bubbles collapsing within the spatial and temporal resolutions of 40 μm and 0.128 μs, respectively. It is worth noting that the acoustic waves reflected by the stone surface can potentially impact the bubble localization. Based on our measurements, the reflected waves were often much weaker and diverged faster than the direct cavitation waves and thus did not affect localization results. Same as other localization-based super-resolution techniques, the signal-to-noise ratio eventually determines the localization accuracy of 3D-SRPCM [37]. Moreover, increasing the transducer frequency can also improve the spatial resolution of 3D-SRPCM, with the potential cost of imaging depth.

3D-SRPCM has great potential for clinical translation with the clinically relevant imaging depth, clear image background,

Authorized licensed use limited to: Duke University. Downloaded on August 20,2024 at 03:16:54 UTC from IEEE Xplore. Restrictions apply.
© 2024 IEEE. Personal use is permitted, but republication/redistribution requires IEEE permission. See https://www.ieee.org/publications/rights/index.html for more information.

This article has been accepted for publication in IEEE Transactions on Ultrasonics, Ferroelectrics, and Frequency Control. This is the author's version which has not been fully edited and content may change prior to final publication. Citation information: DOI 10.1109/TUFFC.2024.3443781

dual-modal imaging capability, and near real-time feedback, which are critically important in guiding urologists for maximizing treatment efficiency. However, limited by the image contrast, 3D-SRPCM cannot be used to evaluate the tissue damage during LL. Integrating 3D-SRPCM with photoacoustic imaging with internal light illumination can potentially provide real-time feedback on tissue damage [25]. It is worth noting that the speed of sound heterogeneity in vivo will affect the localization accuracy of 3D-SRPCM, and more studies are needed to understand the localization resolution demanded for practical clinical benefit. Another important improvement of 3D-SRPCM will focus on providing real-time feedback of cavitation activities for each laser pulse during clinical procedure, which is critically important in guiding urologists for maximum efficiency. Currently, we can achieve a 3D-SRPCM frame rate of 10 Hz with an FOV of 8×8×8 mm^3, which can be accelerated to accommodate higher lase pulse rates by optimizing data processing pipeline, such as using the curving fitting method to identify the bubble collapse time [38].

V. Conclusion

In this work, we have presented a 3D-SRPCM system with a 2D transducer array, which can monitor the cavitation activities during LL treatment of stones. 3D-SRPCM provides the localization of each cavitation center and bubble collapse time with high spatial-temporal accuracy. Particularly, a particle-tracking-based cavitation localization method was adopted to achieve super-resolution reconstruction of the cavitation positions, with an average accuracy of ~40 μm. Moreover, we developed a GPU-accelerated page-wise sparse-matrix-multiplication-based reconstruction method which aims to provide near real-time feedback during LL treatment. We validated the 3D-SRPCM results using high-speed camera in both free-space water and in a space-constrained kidney phantom. We quantified the stone damage by using OCT and analyzed the correlation between the cavitation characteristics with the stone damage. Collectively, we have demonstrated the feasibility of high-resolution 3D-SRPCM for cavitation mapping during LL. We expect to apply our method to optimize the clinical stone treatment and improve the patient outcome.

Acknowledgment

The authors thank Dornier MedTech for providing the H Solvo laser used in this study. This work was partially sponsored by the United States National Institutes of Health (NIH) grants R21EB027981, R21 EB027304, RF1 NS115581, R01 NS111039, R01 EB028143, R01DK139109; The United States National Science Foundation (NSF) CAREER award 2144788; Duke University Pratt Beyond the Horizon Grant; Eli Lilly Research Award Program; and Chan Zuckerberg Initiative Grant (2020-226178).

References

[1] Z. Kirkali, R. Rasooly, R. A. Star, and G. P. Rodgers, "Urinary Stone Disease: Progress, Status, and Needs," *Urology,* vol. 86, no. 4, pp. 651-653, 2015/10/01/ 2015, doi: https://doi.org/10.1016/j.urology.2015.07.006.

[2] C. D. Scales, Jr., G. E. Tasian, A. L. Schwaderer, D. S. Goldfarb, R. A. Star, and Z. Kirkali, "Urinary Stone Disease: Advancing Knowledge, Patient Care, and Population Health," (in eng), *Clin J Am Soc Nephrol,* vol. 11, no. 7, pp. 1305-1312, Jul 7 2016, doi: 10.2215/cjn.13251215.

[3] M. M. Elhilali, S. Badaan, A. Ibrahim, and S. Andonian, "Use of the Moses Technology to Improve Holmium Laser Lithotripsy Outcomes: A Preclinical Study," (in eng), *J Endourol,* vol. 31, no. 6, pp. 598-604, Jun 2017, doi: 10.1089/end.2017.0050.

[4] A. H. Aldoukhi, W. W. Roberts, T. L. Hall, and K. R. Ghani, "Holmium Laser Lithotripsy in the New Stone Age: Dust or Bust?," (in eng), *Front Surg,* vol. 4, p. 57, 2017, doi: 10.3389/fsurg.2017.00057.

[5] B. R. Matlaga *et al.*, "Ureteroscopic Laser Lithotripsy: A Review of Dusting vs Fragmentation with Extraction," (in eng), *J Endourol,* vol. 32, no. 1, pp. 1-6, Jan 2018, doi: 10.1089/end.2017.0641.

[6] T. Reeves, S. Griffin, A. Pietropaolo, and B. K. Somani, "Feasibility of dusting and pop-dusting using high-power (100W) Holmium YAG (Ho:YAG) laser in treatment of paediatric stones: results of first worldwide clincial study," (in eng), *Cent European J Urol,* vol. 72, no. 4, pp. 398-401, 2019, doi: 10.5173/ceju.2019.0009.

[7] D. S. Ho *et al.*, "The Role of Cavitation in Energy Delivery and Stone Damage During Laser Lithotripsy," (in eng), *J Endourol,* vol. 35, no. 6, pp. 860-870, Jun 2021, doi: 10.1089/end.2020.0349.

[8] J. Chen *et al.*, "Cavitation Plays a Vital Role in Stone Dusting During Short Pulse Holmium:YAG Laser Lithotripsy," (in eng), *J Endourol,* vol. 36, no. 5, pp. 674-683, May 2022, doi: 10.1089/end.2021.0526.

[9] M. Mohammadzadeh, J. M. Mercado, and C.-D. Ohl, "Bubble Dynamics in Laser Lithotripsy," *Journal of Physics: Conference Series,* vol. 656, no. 1, p. 012004, 2015/11/01 2015, doi: 10.1088/1742-6596/656/1/012004.

[10] P. Zhong, H. L. Tong, F. H. Cocks, M. S. Pearle, and G. M. Preminger, "Transient cavitation and acoustic emission produced by different laser lithotripters," (in eng), *J Endourol,* vol. 12, no. 4, pp. 371-8, Aug 1998, doi: 10.1089/end.1998.12.371.

[11] A. V. Telichko, T. Lee, M. Jakovljevic, and J. J. Dahl, "Passive Cavitation Mapping by Cavitation Source Localization From Aperture-Domain Signals-Part I: Theory and Validation Through Simulations," (in eng), *IEEE Trans Ultrason Ferroelectr Freq Control,* vol. 68, no. 4, pp. 1184-1197, Apr 2021, doi: 10.1109/tuffc.2020.3035696.

[12] T. Li, T. D. Khokhlova, O. A. Sapozhnikov, M. O'Donnell, and J. H. Hwang, "A new active cavitation mapping technique for pulsed HIFU applications--bubble Doppler," (in eng), *IEEE Trans Ultrason Ferroelectr Freq Control,* vol. 61, no. 10, pp. 1698-708, Oct 2014, doi: 10.1109/tuffc.2014.006502.

Authorized licensed use limited to: Duke University. Downloaded on August 20,2024 at 03:16:54 UTC from IEEE Xplore. Restrictions apply.
© 2024 IEEE. Personal use is permitted, but republication/redistribution requires IEEE permission. See https://www.ieee.org/publications/rights/index.html for more information.

This article has been accepted for publication in IEEE Transactions on Ultrasonics, Ferroelectrics, and Frequency Control. This is the author's version which has not been fully edited and content may change prior to final publication. Citation information: DOI 10.1109/TUFFC.2024.3443781

[13] M. Wan *et al.*, "Acoustic methods for cavitation mapping in biomedical applications," *Journal of Physics: Conference Series,* vol. 656, no. 1, p. 012007, 2015/11/01 2015, doi: 10.1088/1742-6596/656/1/012007.

[14] P. Reinke, T. Beckmann, C. Ahlers, J. Ahlrichs, L. Hammou, and M. Schmidt, "High-Speed Digital Photography of Vapor Cavitation in a Narrow Gap Flow," *Fluids,* vol. 8, no. 2, p. 44, 2023. [Online]. Available: https://www.mdpi.com/2311-5521/8/2/44.

[15] G. Xiang *et al.*, "Dissimilar cavitation dynamics and damage patterns produced by parallel fiber alignment to the stone surface in holmium:yttrium aluminum garnet laser lithotripsy," *Physics of Fluids,* vol. 35, no. 3, 2023, doi: 10.1063/5.0139741.

[16] M. Gyongy and C. C. Coussios, "Passive Spatial Mapping of Inertial Cavitation During HIFU Exposure," *IEEE Transactions on Biomedical Engineering,* vol. 57, no. 1, pp. 48-56, 2010, doi: 10.1109/TBME.2009.2026907.

[17] S. J. Norton, B. J. Carr, and A. J. Witten, "Passive imaging of underground acoustic sources," *The Journal of the Acoustical Society of America,* vol. 119, no. 5, pp. 2840-2847, 2006, doi: 10.1121/1.2188667.

[18] M. D. Gray *et al.*, "Dual-Array Passive Acoustic Mapping for Cavitation Imaging With Enhanced 2-D Resolution," *IEEE Transactions on Ultrasonics, Ferroelectrics, and Frequency Control,* vol. 68, no. 3, pp. 647-663, 2021, doi: 10.1109/TUFFC.2020.3019573.

[19] M. Gyongy, M. Arora, J. A. Noble, and C. C. Coussios, "Use of passive arrays for characterization and mapping of cavitation activity during HIFU exposure," in *2008 IEEE Ultrasonics Symposium*, 2-5 Nov. 2008 2008, pp. 871-874, doi: 10.1109/ULTSYM.2008.0210.

[20] K. J. Haworth, K. B. Bader, K. T. Rich, C. K. Holland, and T. D. Mast, "Quantitative Frequency-Domain Passive Cavitation Imaging," (in eng), *IEEE Trans Ultrason Ferroelectr Freq Control,* vol. 64, no. 1, pp. 177-191, Jan 2017, doi: 10.1109/tuffc.2016.2620492.

[21] C. D. Arvanitis, C. Crake, N. McDannold, and G. T. Clement, "Passive Acoustic Mapping with the Angular Spectrum Method," (in eng), *IEEE Trans Med Imaging,* vol. 36, no. 4, pp. 983-993, Apr 2017, doi: 10.1109/tmi.2016.2643565.

[22] M. Li, G. Sankin, T. Vu, J. Yao, and P. Zhong, "Tri-modality cavitation mapping in shock wave lithotripsy," (in eng), *J Acoust Soc Am,* vol. 149, no. 2, p. 1258, Feb 2021, doi: 10.1121/10.0003555.

[23] M. Li *et al.*, "Time-Resolved Passive Cavitation Mapping Using the Transient Angular Spectrum Approach," *IEEE Transactions on Ultrasonics, Ferroelectrics, and Frequency Control,* vol. 68, no. 7, pp. 2361-2369, 2021, doi: 10.1109/TUFFC.2021.3062357.

[24] M. Li, G. Sankin, T. Vu, Y. Jing, P. Zhong, and J. Yao, "Three-dimensional cavitation mapping in shock wave and laser lithotripsy," *The Journal of the Acoustical Society of America,* vol. 150, no. 4_Supplement, pp. A330-A330, 2021, doi: 10.1121/10.0008470.

[25] M. Li *et al.*, "Simultaneous Photoacoustic Imaging and Cavitation Mapping in Shockwave Lithotripsy," (in eng), *IEEE Trans Med Imaging,* vol. 39, no. 2, pp. 468-477, Feb 2020, doi: 10.1109/tmi.2019.2928740.

[26] G. Y. Hou *et al.*, "Sparse matrix beamforming and image reconstruction for 2-D HIFU monitoring using harmonic motion imaging for focused ultrasound (HMIFU) with in vitro validation," (in eng), *IEEE Trans Med Imaging,* vol. 33, no. 11, pp. 2107-17, Nov 2014, doi: 10.1109/tmi.2014.2332184.

[27] B. Heiles *et al.*, "Ultrafast 3D Ultrasound Localization Microscopy Using a 32 × 32 Matrix Array," (in eng), *IEEE Trans Med Imaging,* vol. 38, no. 9, pp. 2005-2015, Sep 2019, doi: 10.1109/tmi.2018.2890358.

[28] M. Gyöngy and C. C. Coussios, "Passive cavitation mapping for localization and tracking of bubble dynamics," (in eng), *J Acoust Soc Am,* vol. 128, no. 4, pp. El175-80, Oct 2010, doi: 10.1121/1.3467491.

[29] E. Esch, W. N. Simmons, G. Sankin, H. F. Cocks, G. M. Preminger, and P. Zhong, "A simple method for fabricating artificial kidney stones of different physical properties," *Urological Research,* vol. 38, no. 4, pp. 315-319, 2010/08/01 2010, doi: 10.1007/s00240-010-0298-x.

[30] J.-P. v. Brakel. "Robust peak detection algorithm using z-scores." https://stackoverflow.com/questions/22583391/peak-signal-detection-in-realtime-timeseries-data (accessed 2014).

[31] H. A. S. Kamimura *et al.*, "Real-Time Passive Acoustic Mapping Using Sparse Matrix Multiplication," (in eng), *IEEE Trans Ultrason Ferroelectr Freq Control,* vol. 68, no. 1, pp. 164-177, Jan 2021, doi: 10.1109/tuffc.2020.3001848.

[32] C. Cabriel *et al.*, "Combining 3D single molecule localization strategies for reproducible bioimaging," (in eng), *Nat Commun,* vol. 10, no. 1, p. 1980, Apr 30 2019, doi: 10.1038/s41467-019-09901-8.

[33] B. Heiles, A. Chavignon, V. Hingot, P. Lopez, E. Teston, and O. Couture, "Performance benchmarking of microbubble-localization algorithms for ultrasound localization microscopy," *Nature Biomedical Engineering,* vol. 6, no. 5, pp. 605-616, 2022/05/01 2022, doi: 10.1038/s41551-021-00824-8.

[34] R. Parthasarathy, "Rapid, accurate particle tracking by calculation of radial symmetry centers," *Nature Methods,* vol. 9, no. 7, pp. 724-726, 2012/07/01 2012, doi: 10.1038/nmeth.2071.

[35] C. Demené *et al.*, "Spatiotemporal Clutter Filtering of Ultrafast Ultrasound Data Highly Increases Doppler and fUltrasound Sensitivity," (in eng), *IEEE Trans Med Imaging,* vol. 34, no. 11, pp. 2271-85, Nov 2015, doi: 10.1109/tmi.2015.2428634.

[36] S. Tran *et al.*, "Development of an optically transparent kidney model for laser lithotripsy

Authorized licensed use limited to: Duke University. Downloaded on August 20,2024 at 03:16:54 UTC from IEEE Xplore. Restrictions apply.
© 2024 IEEE. Personal use is permitted, but republication/redistribution requires IEEE permission. See https://www.ieee.org/publications/rights/index.html for more information.

This article has been accepted for publication in IEEE Transactions on Ultrasonics, Ferroelectrics, and Frequency Control. This is the author's version which has not been fully edited and content may change prior to final publication. Citation information: DOI 10.1109/TUFFC.2024.3443781

research," *BJU International,* vol. 132, no. 1, pp. 36-39, 2023, doi: https://doi.org/10.1111/bju.16015.

[37] P. Zhang, L. Li, L. Lin, J. Shi, and L. V. Wang, "In vivo superresolution photoacoustic computed tomography by localization of single dyed droplets," *Light: Science & Applications,* vol. 8, no. 1, p. 36, 2019/04/03 2019, doi: 10.1038/s41377-019-0147-9.

[38] P. Song *et al.*, "Improved Super-Resolution Ultrasound Microvessel Imaging With Spatiotemporal Nonlocal Means Filtering and Bipartite Graph-Based Microbubble Tracking," (in eng), *IEEE Trans Ultrason Ferroelectr Freq Control,* vol. 65, no. 2, pp. 149-167, Feb 2018, doi: 10.1109/tuffc.2017.2778941.

Authorized licensed use limited to: Duke University. Downloaded on August 20,2024 at 03:16:54 UTC from IEEE Xplore. Restrictions apply.
© 2024 IEEE. Personal use is permitted, but republication/redistribution requires IEEE permission. See https://www.ieee.org/publications/rights/index.html for more information.